Electron Emission from Amorphous Solid Water Induced by Passage of Energetic Protons and Fluorine Ions

L. H. Toburen,[a,1] S. L. McLawhorn,[a] R. A. McLawhorn,[a] K. D. Carnes,[b] M. Dingfelder[a] and J. L. Shinpaugh[a]

[a] Department of Physics, East Carolina University, Greenville, North Carolina 27858; and [b] J. R. Macdonald Laboratory, Department of Physics, Kansas State University, Manhattan, Kansas 66506

Toburen, L. H., McLawhorn, S. L., McLawhorn, R. A., Carnes, K. D., Dingfelder, M. and Shinpaugh, J. L. Electron Emission from Amorphous Solid Water Induced by Passage of Energetic Protons and Fluorine Ions. *Radiat. Res.* 174, 107–118 (2010).

Absolute doubly differential electron emission yields were measured from thin films of amorphous solid water (ASW) after the transmission of 6 MeV protons and 19 MeV (1 MeV/nucleon) fluorine ions. The ASW films were frozen on thin (1-μm) copper foils cooled to approximately 50 K. Electrons emitted from the films were detected as a function of angle in both the forward and backward direction and as a function of the film thickness. Electron energies were determined by measuring the ejected electron time of flight, a technique that optimizes the accuracy of measuring low-energy electron yields, where the effects of molecular environment on electron transport are expected to be most evident. Relative electron emission yields were normalized to an absolute scale by comparison of the integrated total yields for proton-induced electron emission from the copper substrate to values published previously. The absolute doubly differential yields from ASW are presented along with integrated values, providing single differential and total electron emission yields. These data may provide benchmark tests of Monte Carlo track structure codes commonly used for assessing the effects of radiation quality on biological effectiveness. © 2010 by Radiation Research Society

INTRODUCTION

The biological effectiveness of different types of ionizing radiation is generally attributed to differences in the spatial properties of the products of interactions of the incident particles and resulting secondary electrons. Many different models have been developed to describe the spatial patterns of energy deposition, from simple concepts of linear energy transfer (LET) (*1–3*), to average track models (*4–6*), to the more detailed methods based on event-by-event Monte Carlo models of fast charged-particle tracks (*7–16*). These latter models, which couple the evolution of physical tracks with the subsequent chemical and biochemical reactions, have been used successfully in many areas of radiation biology, including the prediction of damage patterns in the DNA of mammalian cells and tissues (*17–21*). There is an increasing emphasis on the effects of multiply damaged DNA sites (*22–26*) that are generally produced by secondary electron track ends. Interpretation of this clustered damage by Monte Carlo models requires accurate estimates of low-energy electron transport involving elastic and inelastic electron scattering, where models of electron interaction cross sections are most uncertain. It is therefore important to assess the accuracy with which one can assess effects of these theoretical uncertainties on the energies and yields of electrons undergoing the transport process.

The interaction cross sections used in Monte Carlo models of electron transport are generally obtained from theoretical models of the elastic and inelastic interactions of ions and electrons with condensed-phase material (*27–30*); measurements of such cross sections for the condensed phase are extremely difficult, although substantial progress has been made [e.g. refs. (*31–33*)]. The theoretical models used for calculating cross sections are easily defended for particles of intermediate and high energies, where ion or electron velocities are considerably larger than those of the bound electrons of the media, but they are often less accurate for low-velocity electrons, i.e., for electrons with energies less than a few hundred electron volts. The current work was designed to provide benchmark data for assessing low-energy electron transport in condensed water, the surrogate medium used in most Monte Carlo codes for tissue.

To study electron transport in condensed phase, we introduce the initial electron energy distribution within thin films of the medium of interest by the passage of fast ions. The primary distribution of electrons then scatters within the material, losing energy as electrons slow until they are either stopped within the material or exit the surface of the thin foil. The spectra of exiting

[1] Address for correspondence: Department of Physics, East Carolina University, Greenville, NC 27858; e-mail: toburenl@ecu.edu.

electrons reflect information on the characteristics of electron elastic and inelastic scattering in the medium as well as effects of surface potentials; the latter is generally observed for electron energies less than a few eV (*34*). The incident ions used in this study have sufficient velocity that their interactions can be described accurately within the framework of a first Born approximation (*28, 35, 36*), and the foils used are sufficiently thin that the ions lose only a small fraction of their incident energy (i.e., the stopping power changes by less than a few percent) in traversing the foils (*37–39*). In contrast, electrons with energies as high as 1 keV have mean free paths of the order of 3 nm or less (*40*); thus the thickness of 200 monolayers of frozen water (35 to 40 nm) is "thick" relative to the majority of the secondary electrons generated by the transmitted ion. This ensures that the observed spectra are representative of electron interactions in frozen water and not from the copper substrate.

This study continues work initiated at Pacific Northwest National Laboratory (PNNL) nearly two decades ago. The basic features of the apparatus and the experimental technique were first described for the measurement of electron emission from thin carbon foils by fast protons at PNNL (*41*). The target foil holder was subsequently attached to a cryogenically cooled cold finger and initial data were presented for frozen hydrocarbons (*42, 43*). Subsequent to moving the equipment to East Carolina University (ECU), relative electron yields from ASW were measured and strong effects of target charging on the spectra of ejected electrons were found (*44*). This effect caused decreased yields for low-energy electrons; the extent of the decreased yield, i.e., the low-energy spectral cut-off, increased with electron energy as the ASW film thickness increased. A comparison of these emission spectra as a function of foil thickness with the results of Monte Carlo calculations indicated divergences from the model calculations by as much as a factor of five, with the model predictions being larger than measured yields and the largest differences being for electron energies less than a few tens of eV. For ejected electron energies larger than about 100 eV, good agreement in the shape of the spectra between experiment and model calculations was observed; these measurements were limited to 2 MeV proton impact and to relative electron emission yields. As the literature on the structure of ASW increased (*45–48*), it was clear that the method of introducing water vapor to be frozen could have a strong effect on the structure of ASW, particularly on its density/porosity. This, combined with a collaborative effort with colleagues at Kansas State University (KSU) focusing on absolute doubly differential electron yields from metal substrates (*49*), encouraged us to reopen the study of electron emission from ASW. With the additional capabilities of the accelerator at KSU (higher

energy and heavier particles), the study of electron transport in ASW was extended to 6 MeV protons and 19 MeV fluorine ions (1 MeV/nucleon). We introduced the water vapor in a "background" dosing manner, which greatly reduced the effect of target charging on ejected electron yields. The new calibration technique used for copper foils was then applied to obtain absolute values for the measured yields, and measurements were extended to the heavy ion fluorine to explore effects of a densely ionizing ion on electron yields.

EXPERIMENTAL METHODS

The basic features of the experimental target chamber are shown in Fig. 1; additional details are available in refs. (*41–43*) and in the dissertations of Christou[2] and McLawhorn.[3] The ion beam was accelerated, pulsed, focused and energy selected via standard accelerator beam elements and spatially defined by adjustable 4-jaw slits (not shown) before it reached the ultra-high vacuum (UHV) chamber. The beam then entered the measurement chamber through the flange shown at the top of the figure and passed through two collimators approximately 1 mm in diameter followed by a third collimator of slightly larger diameter that could be biased to reduce background electrons produced by ion interactions with the defining collimators. The beam then passed through the target foil mounted on the cold finger of a helium refrigerator at the center of the chamber and was collected in a Faraday cup (not shown) located in the UHV port at the bottom of the figure. The adjustable 4-jaw slit assembly located prior to the chamber was used to limit the beam intensity to that necessary for single particle counting. In addition to the Faraday cup, an electron multiplier positioned at 20° to the incident beam direction and biased to reject secondary electrons was used to monitor the intensity of the Rutherford scattered ion beam when the beam current was too small to be measured by the Faraday cup (and the intensity was too large to be measured by a single particle detector at 0°). For electron spectral counting the beam intensity was reduced to the order of picoamperes or less to limit the possibility of more than one electron reaching the electron detector per incident ion pulse. This small particle fluence also limited any loss of target material from ion beam sputtering; i.e., no time or integrated current dependences were noted in spectra yields of electrons from the ASW targets.

The UHV chamber was constructed of nonmagnetic stainless steel with two layers of magnetic shielding inside the chamber to reduce the ambient magnetic fields in the interaction region. Magnetic fields were reduced to the order of 0.1 μT (1 mG) near the center of the chamber using a small current in a set of external coils to complement the effects of the magnetic shielding. The custom-made cylindrical UHV chamber has an outer diameter of 48 cm, an inner diameter of 44.5 cm, and a height of 36 cm. The chamber is pumped by turbomolecular and titanium sublimation pumps leading to an ultimate vacuum of approximately 1.5×10^{-7} Pa (~1×10^{-9} Torr). At this vacuum level a monolayer of impurities could be absorbed on the target foil in about 1000 s (~17 min) from bombardment of
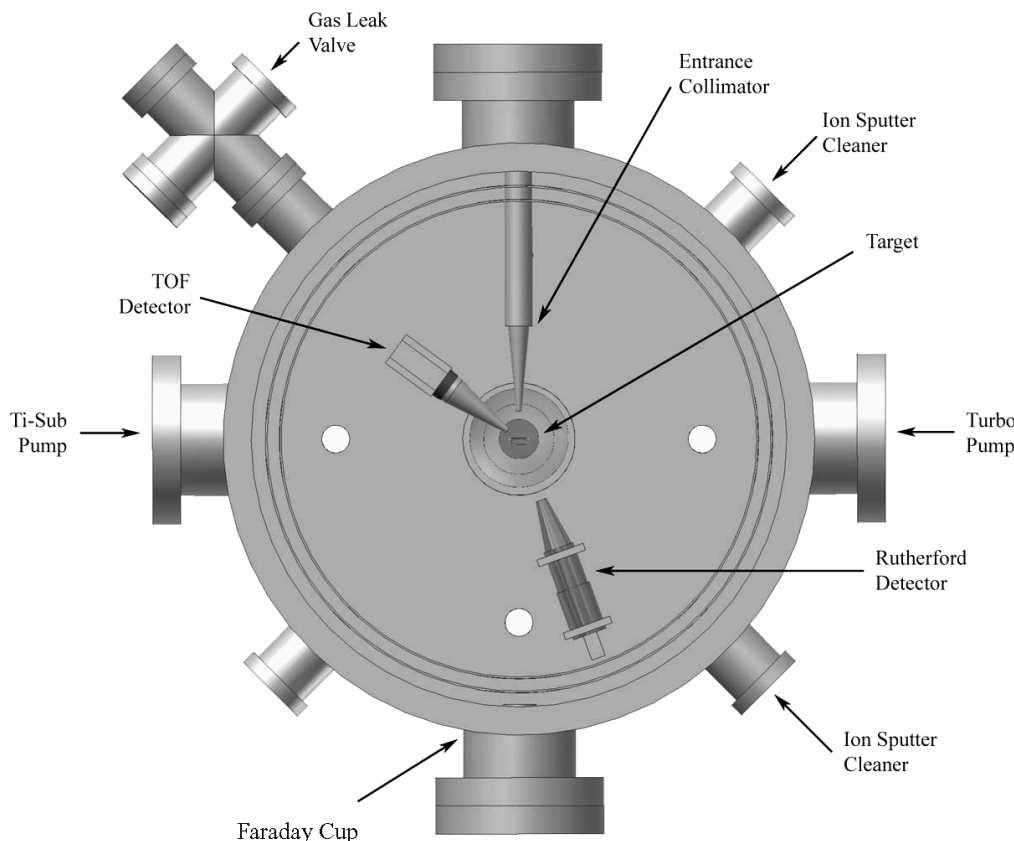
FIG. 1. Schematic representation of the experimental chamber as viewed from the top (chamber lid removed). The general dimensions of the chamber are outer diameter 48 cm, inner diameter 44.5 cm, and height approximately 36 cm.

atoms/molecules in the residual atmosphere of the chamber, assuming a sticking fraction of one (50). The target could be sputter cleaned on both sides of the foil using ion-beam guns located at ±45° to the target, as indicated in Fig. 1; a flash heater at the base of the target also allows target heating to about 450 K for driving off low vapor pressure contaminants. Target cleaning is continued until the measured spectra of ejected electrons do not change with additional sputter cleaning. With each spectrum requiring only a few minutes to acquire, several spectra could be obtained between target cleanings when clean metal targets were studied. For the study of ASW the target foil holder is attached via a sapphire electrical insulator to a cold finger cooled by a closed-cycle helium refrigerator mounted at the center of the chamber. Thermocouples at the base of the cold finger and at the base of the target holder provide temperature monitoring during target cooling. For ASW target preparation the copper foil substrate was first sputter cleaned with 5 keV neon ions and then the target cooled to less than about 50 K as determined by the thermocouple at the base of the target holder. By using neon ions instead of the more commonly used argon ions, one could clean the surface at low temperatures without freezing the ions on the surface; sputter cleaning the cold target immediately prior to freezing the water target did not make observable changes in the electron spectra over cleaning prior to cooling the target.

For studies of ASW, water vapor was introduced into the UHV chamber through a gas leak valve at the 135° port, as shown in Fig. 1, where it was frozen on a 1-μm-thick polycrystalline copper substrate held at approximately 50 K. Water ice frozen at temperatures less than about 135 K takes on an amorphous form, in many respects similar to liquid water (45); the phase transition between amorphous and crystalline water takes place between 125 K and 145 K. In the earlier work of Christou,[2] water vapor had been introduced from a

vacuum port located at 45° relative to the forward direction of the ion beam with direct line of sight to the front of the target foil. That freezing technique was similar to that shown to lead to the development of microchannels in the water foil (47), which could have effects on the electron spectra. To examine possible effects of target structure on the emission spectra, in the measurements reported here the water vapor was introduced in a diffuse manner as a small increase in the chamber pressure. As will be shown below, this method of background dosing resulted in greatly reduced target charging being observed in the spectra of electrons from the ASW foil, but the general trends of the spectra are in good agreement with the composite thickness dependence of the earlier data when the differences expected from the change in proton energy 2 MeV to 6 MeV were considered.

Water vapor was introduced via the leak valve on the 135° port at chamber pressures less than about 1.3×10^{-5} Pa (1×10^{-7} Torr), resulting in the buildup of the ASW film at somewhat less than 1 monolayer/s. The pressure in the chamber, and thereby the accumulated ASW thickness, was monitored continuously with a sampling rate of 1/s by a computer programmed to record the output of a Bayard-Alpert nude ionization gauge on the UHV chamber. From this rate of deposition and from the general diffuse manner of vapor deposition, we feel that the deposition represents the "background" dosing conditions described by Kimmel et al. (46–48), resulting in a microporous ASW film with approximate density 0.6 g/cm³.

The time-of-flight (TOF) electron detector shown in Fig. 1 is supported from an X, Y, Z and θ manipulator attached to the center flange of the chamber lid (in this cut-away view, the chamber lid is not shown). This manipulator allows for precise alignment of the detector collimator to the beam spot and unimpeded angular motion of the

TOBUREN *ET AL.*

detector from $-10°$ to $+155°$ about the target foil (angles measured clockwise from the forward direction of the ion beam). Electron spectra were normally measured for seven angles from $15°$ to $60°$ and five angles from $115°$ to $155°$. Target structural components and the foil dimensions interfere with measurement near $90°$. The electron time-of-flight detector consists of two chevron-aligned microchannel plates (*51*) with voltages applied such that electrons are accelerated by approximately 50 V from the exit of the grid defining the field-free drift region to the entrance of the electron multiplier. This electron acceleration helps maintain high detection efficiency for even the lowest-energy electrons. In this work the detection efficiency is assumed to be constant for incident electron energies from zero (effectively 50 eV, owing to the applied acceleration potential) to 1 keV. This assumption is in agreement with measurements conducted for similarly manufactured single-channel electron multipliers in our laboratory (*52*) and with the results of Wiza (*51*), who reported a 15% increase in efficiency, and of Müller *et al.* (*53*), who reported a 15% decrease in efficiency with increasing electron energy in this energy range. The absolute efficiency is not of concern because the yields are normalized to measured total yields from metallic copper targets (*49, 54*). The field-free flight distance used in the current measurements was 89.4 mm, which is large relative to the 2.1-mm acceleration region, leading to negligible contributions to the time of flight after electrons exit the field-free region.

To determine the time resolution of the detector system, the beam intensity was reduced and the TOF electron detector was positioned at $0°$. Because the probability of electron detection is much less than one electron per ion within the small solid angle subtended by the detector (2.9×10^{-4} sr), the spectrum at $0°$ is dominated by the incident ion beam, resulting in a measurement of the time profile of the incident ion-beam pulse. For the measurements reported here, the full-width-half-maximum (FWHM) time resolution was approximately 2 ns. The TOF technique provides constant spectral resolution in time; when converted to energy spectra, the energy resolution becomes a function of electron energy. The 2-ns time resolution results in an electron energy resolution of 30 meV at 1 eV (3%), increasing to 0.8 eV at 10 eV (8%) and about 25 eV at 100 eV (25%). Thus, as noted earlier, the TOF technique is optimized for low-energy electron spectroscopy. Structure in the emission spectra at higher electron emission energies, such as Auger transitions at hundreds of eV, are broadened both by energy degradation in the bulk material and by the energy resolution of the TOF system, thereby washing out such structures and often making them effectively indistinguishable from the electron continuum.

RESULTS

An example of the TOF electron emission spectra obtained in this work is shown in Fig. 2. Here the spectra for electron emission at $15°$ are compared for electrons emitted from bare cleaned copper and from 200 monolayers of ASW. In this representation, time zero is defined by the proton peak centered in channel 1688, and the flight time increases by 0.253 ns/channel as the channel numbers decrease relative to the proton peak; the sharply peaked distribution represented by the solid line at the right in Fig. 2 is the measured beam time profile. The actual time zero is about 10 channels to the right of the proton peak because of the time required for the proton to travel from the foil to the detector. The electron energies are calculated from the relationship given by
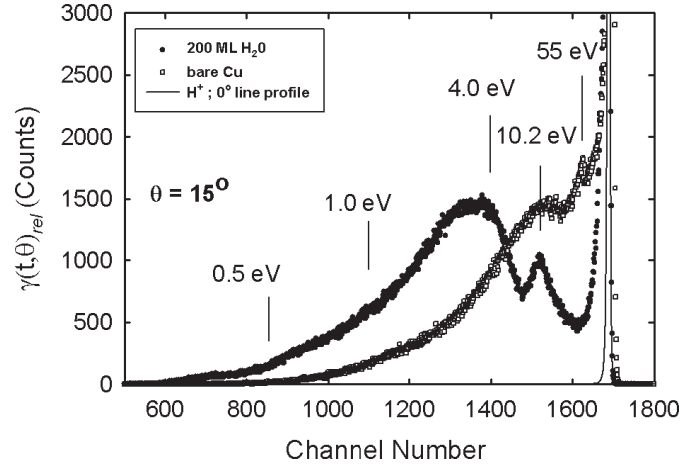

FIG. 2. The time-of flight spectra of electrons ejected at $15°$ from cleaned bare copper ($\square$) and 200 monolayers of ASW ($\bullet$) by 6 MeV protons. Selected electron energies are shown at the channel number representing the corresponding time-of-flight of the electrons; note the nonlinear energy scale. The sharply peaked curve shown as the solid line in channels 1650–1700 is the time profile of the proton beam at $0°$.

$$\varepsilon = \frac{1}{2}mv^2 = \frac{1}{2}m\left(\frac{d}{t}\right)^2, \qquad (1)$$

where m is the electron mass, d is the flight distance, and t is the time of flight determined from the time width of the channel and the number of channels between time zero and the channel representing the time of arrival of the electron. The shape of the time profile of the scattered proton beam merges with the secondary electron spectrum at an electron energy of about 1 keV. This limits the applicable electron energies that can be investigated to no more than 1 keV, even though the effective limit is reached at even lower energies because of the poor energy resolution as the electron energy increases; as mentioned previously, the TOF technique is best suited for electron energies from about 0.1 to 200 eV with the parameters used in this work, e.g. ref. (*55*).

The spectrum for ASW shown in Fig. 2 exhibits a larger yield of low-energy electrons and a smaller yield of higher-energy electrons than the spectrum obtained for copper. Of particular interest in these spectra are the peak superimposed on the time spectrum for ASW at about 10.2 eV and the small peak at about 55 eV in the spectrum of electrons from copper. The peak for ASW has been attributed to autoionization of excited states of the water molecule and has been studied extensively for electron impact by Wilson *et al.* (*56*). The structure in the spectrum of electrons from copper peaking at about 55 eV is attributed to unresolved M-Auger transitions excited in copper.

The time spectra measured for electrons from surfaces can be converted to energy spectra by the relationship
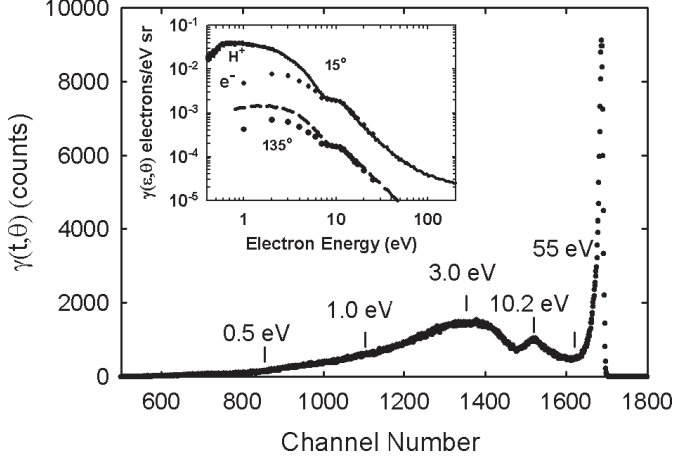
FIG. 3. The time-of flight spectra of electrons ejected at 15° by 6 MeV protons. The inset shows the low-energy portion of the energy distribution derived from TOF spectra at 15° (solid line) and 135° (dashed line) compared to 100 eV electron impact data of Wilson *et al.* (*56*) measured at 135°. The electron impact data were normalized to the proton data at 10 eV.

$$\gamma(\varepsilon,\theta)_{rel} = \frac{N_e t^3}{N_{sp}\Delta_t m d^2}, \qquad (2)$$

where $\gamma(\varepsilon,\theta)_{rel}$ is the relative differential yield per ion, N_e is the number of electrons detected per time channel, t is the total flight time for electrons in channel N_e, N_{sp} is the number of scattered particles detected in the Rutherford scattering detector (provides yields proportional to incoming particle number), Δ_t is the channel width in ns, m is the electron mass, and d is the field-free electron flight distance. To determine the *absolute* yields, the differential yields for the copper target are integrated with respect to emission angle and energy and the total measured yield is normalized to published values (*54*). Since no experimental parameters are changed in freezing water to the copper target and the added thickness is relatively small, this normalization constant is also valid for determining absolute yields for the data from ASW targets. Figure 3 shows the proton-induced TOF spectra for 15° electron emission from a 200 monolayers ASW film along with an insert that shows the comparable absolute differential energy distribution $\gamma(\varepsilon,\theta)$ as a function of the ejected electron energy plotted logarithmically. The 10.2 eV peak in the time spectra washes out in the energy distribution to become a small change in slope. Also shown in the inset are data for 100 eV electron impact taken from Wilson *et al.* (*56*) that have been normalized to the proton impact data at 10 eV. Although the parameters of the electron impact experiment are considerably different, i.e., electron impact data were reported only at 135° emission angle, the incident electron beam was at 135° rather than the 90° impact angle of the protons, and the incident electron beam is of lower velocity than the proton beam, the shape of the spectra in the vicinity of the peak
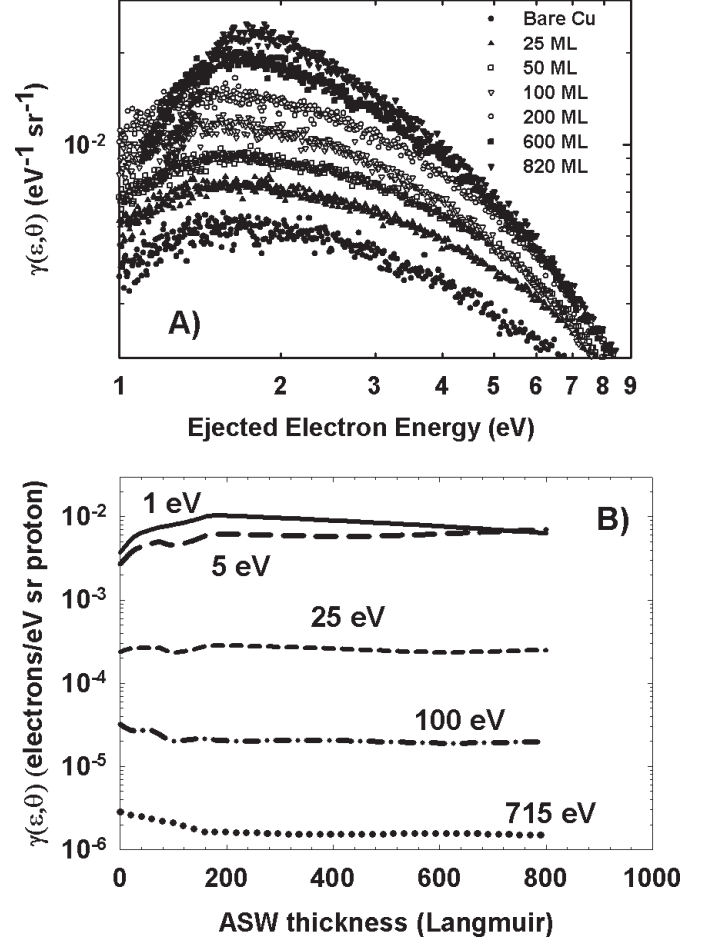

FIG. 4. Electron yields as a function of ASW thickness for low-energy electrons (panel A)and thickness dependence for selected electron energies (panel B). Thicknesses of ASW foils were measured from zero (bare copper, lowest yield with filled squares) to 820 monolayers of ASW (inverted filled triangles). The shift in the threshold to higher electron energies observed in panel A for 600 and 820 monolayers is indicative of foil charging. In panel B, the low-energy electron yields are observed to increase with ASW thickness to about 200 monolayers, whereas high-energy electron yields decrease.

structure is quite similar. This tends to support the interpretation of Wilson *et al.* that the peak at 10–15 eV results from autoionization of the $2a_1{}^{-1}4a_1$ excited state of solid water leading to a final vacancy in one of the valence levels ($1b_2$, $3a_1$ or $1b_1$). The fast electron and proton have similar probabilities in exciting the various valence states of the target water molecules.

Our goal was to measure the absolute differential electron yield representative of electron emission from ASW. Since the ASW is frozen to a copper substrate, the ASW film thickness must be thick relative to the range of the electron energies of interest to ensure that the spectra are representative of ASW. To observe the yield as a function of ASW thickness, measurements were made for target thicknesses from zero (bare cleaned copper) to 820 monolayers. A subset of these measurements is shown in Fig. 4A for electrons emitted at 45°.

The yield increases with ASW thickness with no change in spectral shape until about 400 monolayers. For thicker coverage we see effects of foil charging as the increase in the threshold for electron emission increases. Figure 4B shows the yield for selected electron energies as a function of target thickness. The yield for low-energy electrons first increases, then saturates at about 200 monolayers, whereas at high energies the yield first drops but again appears to saturate at about 200 monolayers. Based on these data we consider the 200-monolayer film to be the best choice for measurements; it is thick relative to electron ranges and is unmodified by target charging. If we assume about 2 Å per monolayer, 200 monolayers of ASW is about 40 nm thick, which is approximately the range of electrons of 1 keV. Very little difference was observed between the integrated total electron yields for 100 monolayers and 200 monolayers, suggesting that saturation might occur at coverage even less than 200 monolayers.

Uncertainties from effects of foil charging, from statistical uncertainties involving low-count rates, and from the general difficulty in reproducibility between runs are compounded in the spectra measured for very low-energy electrons. These uncertainties limit the threshold of reliability to data above 1 eV. It should also be emphasized that the energy threshold for electron emission is angular dependent; the surface potential is normally defined as perpendicular to the foil surface, but the component in the direction of the emitted electron increases as $1/\cos \theta$, resulting in an increasing threshold for electron emission as the angle increases. Thus the spectra at 60° show a larger threshold for emission even though the experimental technique may have a reliability threshold of 1 eV at 15°. Several independent measurements were made at KSU with excellent reproducibility between measurements for ejected electron energies from a few eV to several hundred eV. The results presented in the following sections are averages of multiple runs, and representative uncertainties will be discussed below.

Measured Yields: 6 MeV Protons

The doubly differential electron yields from 200 monolayers of ASW frozen to a sputter cleaned copper substrate are shown in Fig. 5. These data are the averages of two separate runs that were made over 2 months. Uncertainties owing to statistics and differences in spectra from run to run are generally less than 30% for electron energies from 3 eV to 100 eV and increase to as much as a factor of 2 at the lowest energies. The absolute yields were obtained by normalizing the total integrated yields for copper to the values of Koyama *et al.* (*54*) as discussed above. Prominent features of the spectra are the broad maximum (accentuated by the logarithmic energy scale) in the
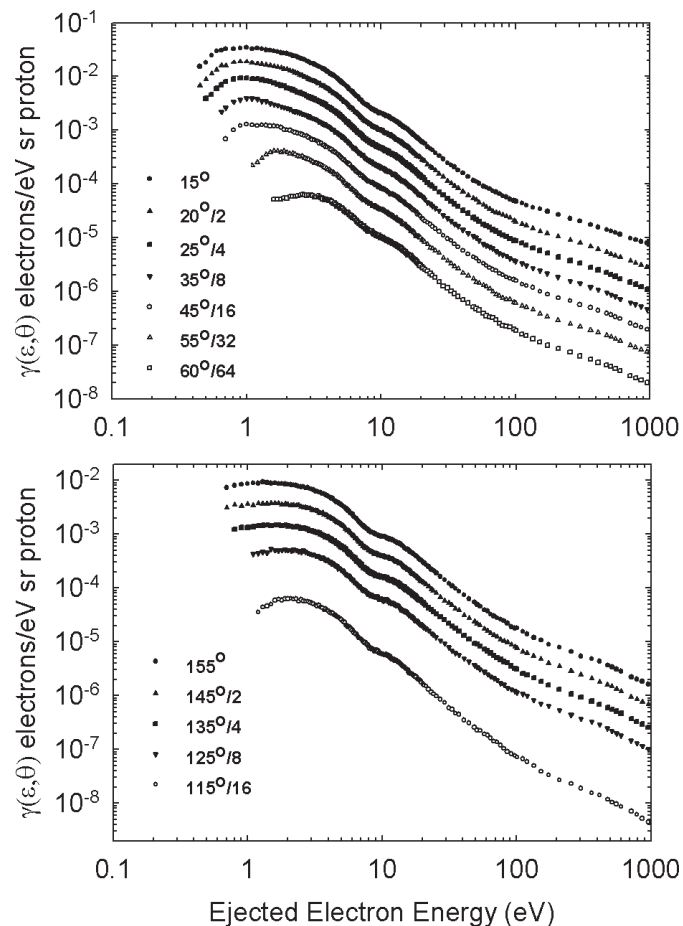

FIG. 5. Doubly differential yield of electrons ejected from 200 monolayers of ASW by 6 MeV proton impact. Points are the average of two independent sets of measurements. Results for the lowest electron energies have been cut off when statistical uncertainties were greater than about a factor of 2. Spectra for different angles have been offset successively by factors of 2 for clarity.

distribution for low-energy electrons (from about 1 to 3 eV depending on emission angle) and the small structure in the spectra for electron energies between about 11 and 15 eV. The latter was observed and described previously (*56*) as resulting from autoionization. The low-energy maximum moves to larger energies as the emission angle increases from 15° in the forward direction and moves to higher energies as the angle decreases from 155° in the backward direction. This is attributed to the larger effect of the surface potential on the low-energy electrons; i.e., the low-energy threshold corresponds to the point at which the component of the electron velocity normal to the surface is insufficient for the electron to escape the surface potential. A plot of the angular distribution for selected ejected electron energies is shown in Fig. 6. The distribution falls off more rapidly than the cosine dependence that we found for a clean copper surface (*49*) for both the low-energy and the higher-energy ejected electrons. This divergence from the expected dependence on $\cos(\theta)$ may be a result of otherwise unobserved charging of the water film as
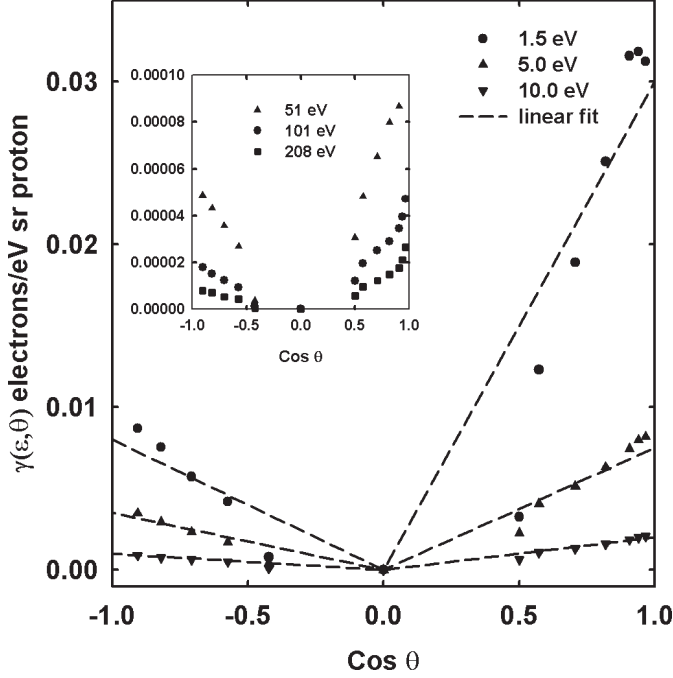
FIG. 6. Angular distributions of doubly differential electron yields for selected electron emission energies. The dashed lines are linear fits through zero to guide the eye. The angular distributions decrease more rapidly than linear with the cosine of the emission angle in contrast to the linearity observed for bare metals (*49*).

FIG. 7. Comparison of the measurements for electron emission at 45° from 200 monolayers of ASW by 6 MeV protons with simulations for 40° and 50° derived from the PARTRAC code modified to track electrons to 1 eV.

electrons are ejected in the insulating ASW film. It appears that the linearity is maintained somewhat better for electrons ejected in the backward direction than the forward direction. Perhaps this is evidence for some asymmetry in the thickness of the foils or is simply a result of the lower electron yields in the backward direction producing less chance of target charging.

The averages are compared to simulations based on the PARTRAC Monte Carlo code in Fig. 7 [for more details on PARTRAC simulations, see refs. (*16*) and (*44*)]. The calculations agree quite well with the measurements for electron energies greater than about 100 eV (within combined statistical uncertainties) but show large differences for lower energies; this comparison shows discrepancies similar to the earlier results for 2 MeV protons and emphasizes the overestimation of the number of low-energy electrons predicted by the transport code after passage of fast protons in water. The model calculations also show some structure similar to the measurement in the region of 10 eV in these distributions, although autoionization in the excited water is not explicitly included in the PARTRAC code. The 10 eV structure in the model calculation is thought to be related to thresholds in the energy loss process related to target structure; this is currently being investigated.

The single differential yield of electrons obtained by integration over emission angle is shown in Fig. 8. The integral was evaluated by the trapezoidal rule with the
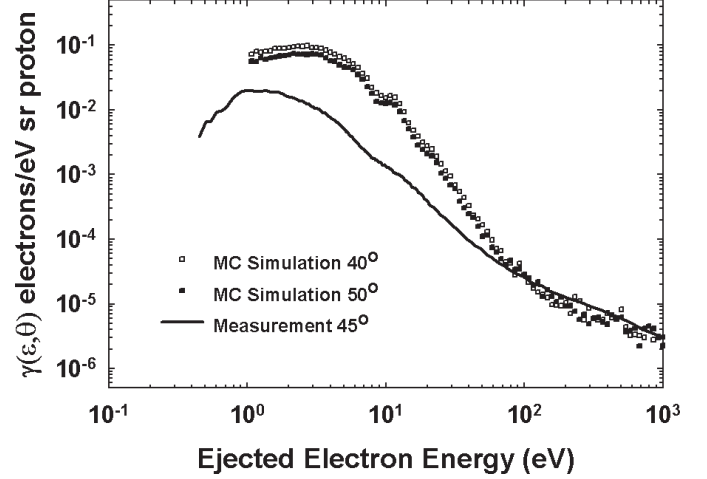
yield at 90° taken as zero, and that at 0 and 180° assumed to be the same as that at 15 and 155°, respectively. Because the integral is weighted by the cosine of the emission angle, the uncertainties introduced by the assumed values at 0 and 180° are considered negligible. In the integrated yields we plotted the spectra to somewhat lower electron energies than we considered reliable in the doubly differential yields. By using a three-point averaging of the data points coupled with the effective averaging of the integration process itself, the integral values have much less statistical fluctuation than the angular data. We also show in the inset in Fig. 8 the single differential yields on linear-linear scales more commonly used in surface studies. Here we see the relative unimportance of electrons with
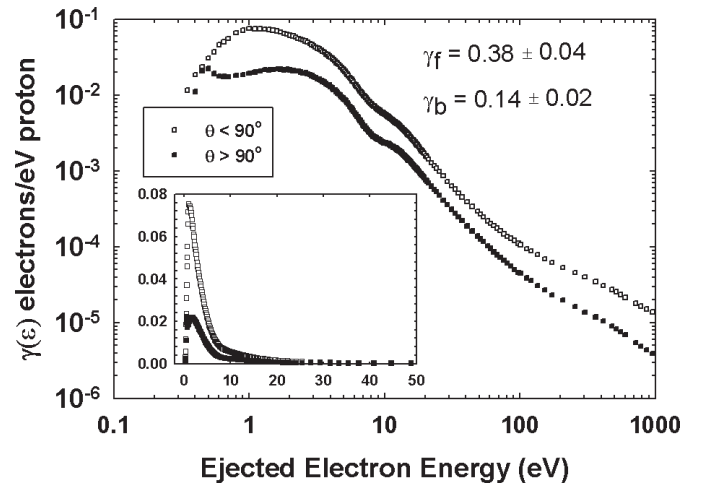

FIG. 8. The integral over emission angle measured for forward (□) and backward angles (■). Also shown as an inset in the lower left of the figure is the linear display generally used in surface science studies. Also shown are the total forward yield γ_f and the total backward yield γ_b obtained from an additional integration over electron energy.

energy less than 1 eV except to show the rapid decrease in yield to zero as the energy decreases. The linear representation also suggests that the contributions to the total yield for electron energies larger than about 30 eV would be negligible. However, we found that about 15% of the total forward yield came from electrons with energies larger than 100 eV. The total forward (γ_f) and backward (γ_b) electron yields obtained by integrating the singly differential spectra over the emission energies are also given in Fig. 8. These total yields have an uncertainty of about 15% based on variations between data sets and depending on the upper limit of the electron energy used in the integration. These yields of γ_b = 0.14 ± 0.02 and γ_f = 0.38 ± 0.04 are smaller than the comparable values from backward emission from clean copper of 0.27 ± 0.01 and are nearly the same as those for forward emission from clean copper of 0.36 ± 0.01 (*49*).

Measured Yields: 1 MeV/nucleon Fluorine Ions

With the higher ion energies available at KSU, heavy ions could be used that did not lose significant energy in passing through the thin films used in these measurements, leading to additional benchmarks for testing electron transport models. For these measurements F^{4+} ions were accelerated to 19 MeV (1 MeV/nucleon) and passed through ASW prepared in the same way as for the proton measurements. The initial secondary electron distributions produced by the fluorine ions within the condensed-phase targets will be different from fast protons owing to the different velocity and charge states of the ions, but the ion energy is still within the "high-energy" range where theoretical methods for ion-molecule cross-section calculations are believed to be accurate. The incident ion will strike the front foil surface as a charge state 4+ ion and will quickly equilibrate to an equilibrium charge state of approximately 6.5+ by electron capture and loss processes (*57*). This changing charge state provides an additional test of the modeling because the instantaneous charge state is a parameter in the theory providing the initial spectrum of electrons released in the medium and because the electron capture and loss process also contributes energetic electrons to the medium traversed. These events are important for track structure codes that might be used, for example, for interpretation of the spatial distribution of energy deposition events initiated by ions used in heavy-ion microbeam studies of molecular and cellular targets or in heavy-ion therapy.

Examples of the measured time-of-flight spectra for electrons emitted at 15° from ASW and bare copper by 6 MeV protons are compared in Fig. 9 to a spectrum for incident 1 MeV/nucleon F^{4+} ions. The fluorine-ion data do not exhibit the clear autoionization structure in the spectra at 10.2 eV for the ASW target that is observed
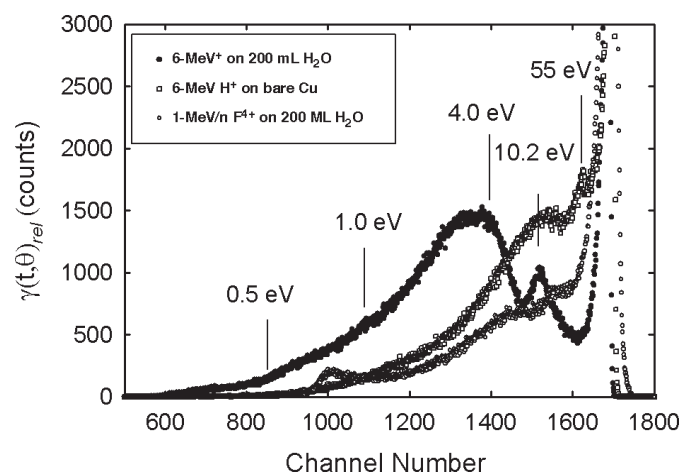

FIG. 9. The time-of-flight spectrum of electrons ejected at 15° from 200 monolayers of ASW by 1 MeV/nucleon F^{4+} ions (○) compared to the spectra measured from bare copper (□) and 200 monolayers of ASW (●) by 6 MeV protons. A new structure is observed in the F^{4+} data at about 0.7 eV; this is attributed to target charging. The autoionization peak observed at about 10 eV in the proton spectrum is missing in the fluorine data.

for proton impact; there appears to be evidence of a very weak structure but not a definitive peak. This lack of a clear autoionization structure in the data for fluorine ions is probably due to a relative increase in the background of continuum electrons from outer-shell ionization induced by the highly charged ions that obscures the structure. With the highly charged, slower fluorine ion, one expects a much higher probability of ionization of the outer shells of the molecular solid. That plus the higher probability of multiple ionization, which would likely decrease the relative autoionization yield, can obscure any autoionization that might be produced in these heavy-ion collisions. The fluorine-ion results do show a new structure in the sub-eV energy range that was not seen in the spectra excited by the faster protons. This structure will be seen below to result from foil charging, which occurs more prominently with these heavy ions than with the 6 MeV protons.

The energy and angular differential electron yields for electron emission at 15° from impact of 1 MeV/nucleon fluorine ions and 6 MeV protons are compared for both copper and ASW targets in Fig. 10. In general the shapes of the spectra are similar for protons and fluorine ions except for kinematic effects. The enhancement of the yields for fluorine ions in the energy range from 200 to 500 eV is expected owing to the distributions of electrons that follow in the "wake" potential of the ion, enhancing the direct ionization electrons (*57*) as well as those electrons stripped from bound states of the ion as it traverses the target material (*58*); in either case the distributions are further broadened by the poor resolution of the TOF system at these high energies. These effects would not be seen in the proton data because the velocity condition for the 6 MeV protons would be well
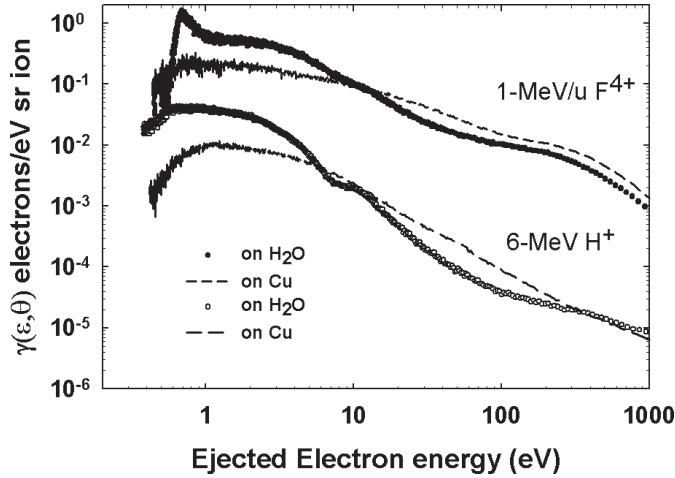
FIG. 10. A comparison of the doubly differential electron yields of electrons ejected at 15° from ASW and copper by incident protons and fluorine ions.

past the energy range shown and beyond the limits of the TOF system. The electron yields from ASW are enhanced relative to the copper target for electron energies below about 10 eV for both protons and fluorine ions and decrease below those of copper for energies above about 10 eV. It may be significant that the crossover occurs at the same electron energy for both protons and fluorine ions, although the total yields are much larger for the fluorine ion. Again, as discussed above, there is only a weak hint of structure in the fluorine-ion-induced spectra near 10 eV, in contrast to the definite structure in the proton data.

The spectra were investigated as a function of ASW thickness to determine the potential effects of target charging on spectral shape. The low-energy portion of a limited selection of measurements is shown in Fig. 11. The low-energy threshold shifts to higher electron energies as the ASW thickness increases. This shift occurs for thinner ASW layers and is somewhat larger than that shown in Fig. 4 for proton impact. In addition, a small peak tends to form above threshold that increases in intensity and energy as the thickness increases; this is most clear in the 135° spectra, although it is also observed in the forward direction. The charging affects the spectra up to nearly 2 eV for the thickest layer we investigated, a point that must be considered for application of the results of these measurements. Based on the thickness dependence measurements for fluorine ions as well as those discussed above for protons, a thickness of 200 monolayers was used for the measurements presented.

In the case of fluorine ions, three independent sets of data were obtained for fluorine ions. As with the proton results, good agreement was observed between data sets, but with fluorine ions the effects of charging limited the reliability to electron energies above about 1.5 eV for emission angles nearly perpendicular to the foil and
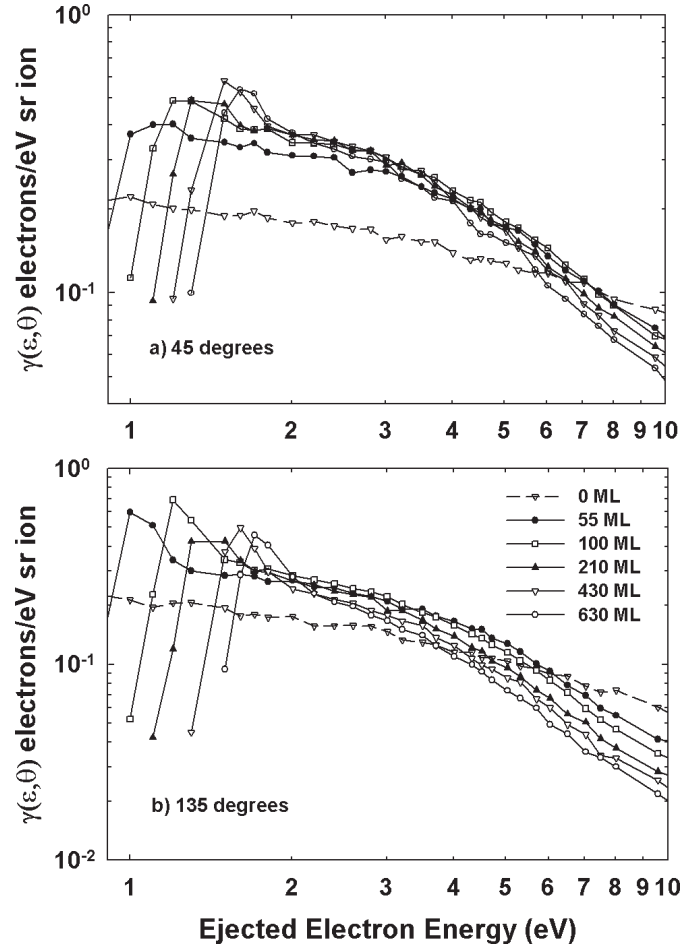

FIG. 11. Thickness dependence of the low-energy electron yields, beginning with bare copper (dashed line) and continuing for selected thicknesses to 630 monolayers of ASW (○) for electrons emitted in the forward direction (upper panel a) and backward direction (lower panel b). For clarity, only a sampling of the full set of thickness measurements is shown. The most important features are the increased yield with increased thickness of ASW observed for electron energies from 1 to about 9 eV and small shifts observed in the low-energy threshold for electrons as the ASW thickness increases; these shifts are considered representative of charging of the target.

larger energies at larger angles. For the fluorine data at energies greater than 1.5 eV, the uncertainties from averaging independent runs and from statistical variations in individual data sets are generally less than about ±20%, which is somewhat better than was obtained for the proton data. The final results for the doubly differential electron yields are shown in Fig. 12, where data for individual angles are offset by factors of two for additional clarity. We have not included data for emission at 115° because these spectra were not well reproduced from run to run, suggesting interference by structural components of the foil holder. Angular distributions of the doubly differential yields are shown in Fig. 13 for selected electron energies from 5 eV to 208 eV. The expected linear dependence of the angular distribution on the cosine of the angle is shown as
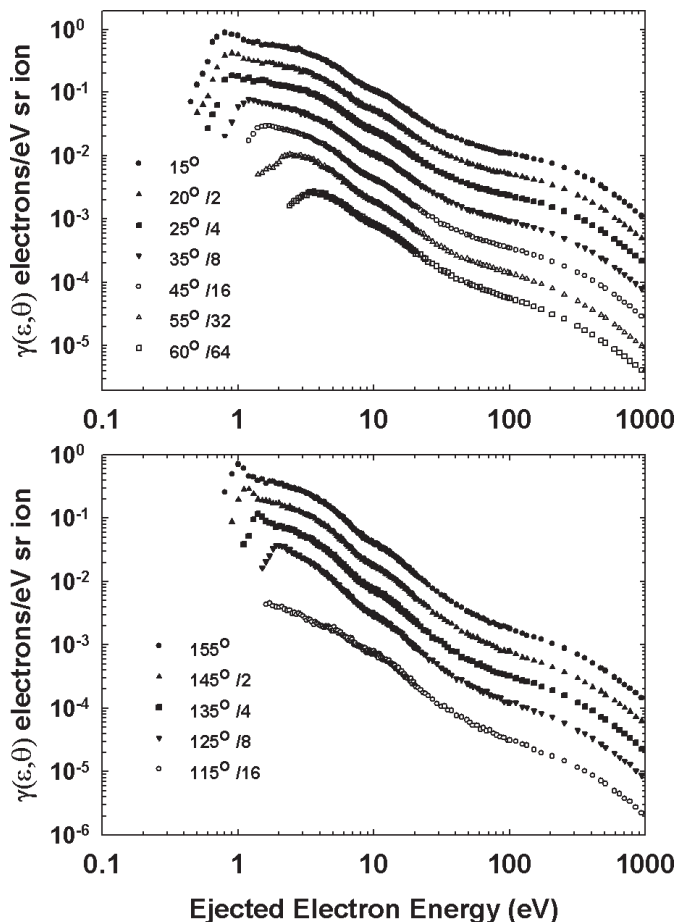
FIG. 12. Yields differential in ejected electron energy and emission angle are shown for electron emission from 200 monolayers of ASW after passage of a 1 MeV/nucleon fluorine ion. Points represent the average of three independent measurements. Spectra for different angles have been offset successively by factors of 2 for clarity.

dashed lines in Fig. 13. The data exhibit some divergence from the linear decrease expected but not as much as was seen above in comparable data for the 6 MeV protons.

The single-differential electron yields for ASW obtained from integration of the doubly differential yields with respect to emission angle are shown in Fig. 14. The low-energy maximum in the spectra for forward angles is somewhat broader than the peak observed for proton impact. This is attributed to the larger effect of foil charging encountered with the fluorine-ion beam. The broad enhancement in the spectra of electrons near the equal velocity criterion occurring for electron energies near 545 eV is observed for both forward and backward scattered electrons. This enhancement is attributed to electrons bound to the fluorine ion that are stripped and scatter from interactions with the target (58) as well as those in the forward direction that are following in the potential wake of the ion (59). The total electron yields for electrons ejected in the forward and backward directions were obtained from integration of the electron
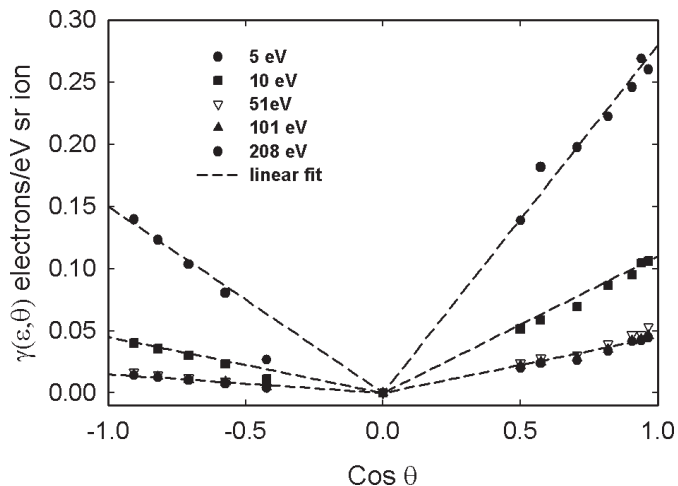

FIG. 13. Angular distributions for electrons of selected energies ejected from ASW by incident 1 MeV/nucleon F^{4+} ions. The dashed lines are linear fits to guide the eye.

spectra shown for electron energies from zero to 1,000 eV. As with the proton data described above, the contribution of high-energy electrons to the total yield can be as much as 30–40% of the electrons ejected by these fast heavy ions for electron energies above 100 eV. This is much more than would be expected based on a linear plot of the yields as shown in the inset in Fig. 14. Although there are few electrons ejected per unit energy at high energies, the range of possible energies is very large.

SUMMARY

Absolute energy and angular differential yields for electrons ejected from the front and back surfaces of amorphous solid water frozen on copper substrates are
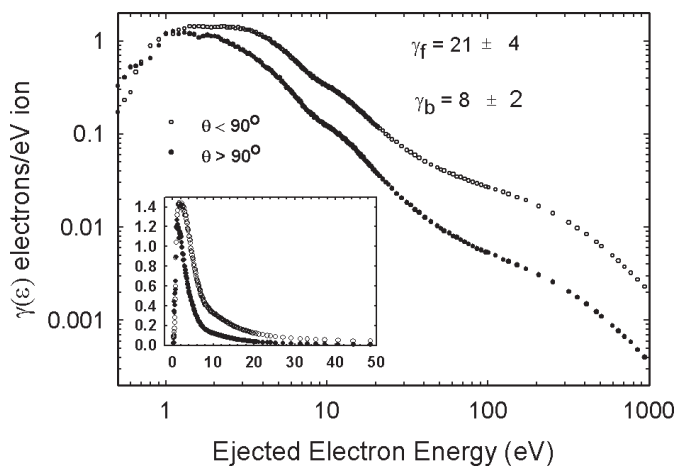

FIG. 14. The energy-differential yield of electrons from ASW after passage of 1 MeV/nucleon fluorine ions. The inset shows a linear-linear plot of the low-energy portion of the emission spectra, a more common representation used in surface science studies. Also shown are the total electron yields in the forward direction γ_f and backward direction γ_b obtained from an integration of the singly differential yields.

presented for interactions of 6 MeV protons and 1 MeV/nucleon fluorine ions. The absolute yields were derived from calibration of the system to total yields measured previously for protons on copper. The ASW foil thicknesses were chosen to be thick relative to the range of the majority of electrons ejected to ensure they exhibit the characteristics of transport in condensed-phase water. Frozen on sputter-cleaned polycrystalline copper foils held at a temperature of approximately 50 K, the ASW foils are amorphous, with characteristics similar to liquid water to serve as a testing base for biophysical models of electron transport in liquid water. For the background dosing methods applied here, the foil structure is expected to be of a random porosity with a density of approximately 0.6 g/cm^3. Yields are measured for electron energies from about 1 eV to about 1 keV for emission at seven angles in the forward direction from 15° to 60° and for five angles in the backward direction from 115° to 155°. The singly differential electron energy spectra and the total electron emission yields are also presented.

REFERENCES

1. R. Blohm and D. Harder, Restricted LET: still a good parameter of radiation quality for electrons and photons. *Radiat. Prot. Dosimetry* **1–4**, 377–381 (1985).

2. I. Yoshikawa, T. Takatsuji, M. Hoshi, J. Takada, T. Kanai, Y. Furusawa, H. Nikjoo and M. Ikenaga, The relative biological effectiveness of accelerated carbon ions with different LET for inducing mitotic crossing over and intragenic reversion of the *white-ivory* allele in *Drosophila* larvae. *Int. J. Radiat. Biol.* **74**, 239–248 (1998).

3. J. A. LaVerne, Track effects of heavy ions in liquid water. *Radiat. Res.* **153**, 487–496 (2000).

4. J. J. Butts and R. Katz, Theory of RBE for heavy ion bombardment of dry enzymes and viruses. *Radiat. Res.* **30**, 855–871 (1967).

5. R. Katz and R. Zachariah, Experimental and theoretical cross sections for *Escherichia coli* mutants B, B/r, and B$_{s-1}$ after heavy-ion irradiation. *Radiat. Res.* **134**, 261–264 (1993).

6. F. A. Cucinotta, R. Katz and J. W. Wilson, Radial distribution of electron spectra from high-energy ions. *Radiat. Environ. Biophys.* **37**, 259–265 (1998).

7. H. Nikjoo, P. O'Neill, D. T. Goodhead and M. Terrissol, Computational modeling of low-energy electron-induced DNA damage by early physical and chemical events. *Int. J. Radiat. Biol.* **71**, 467–483 (1997).

8. S. M. Pimblott, J. A. LaVerne and A. Mozumder, Monte Carlo simulation of range and energy deposition by electrons in gaseous and liquid water. *J. Phys. Chem.* **100**, 8595–8606 (1996).

9. V. Cobut, Y. Frongillo, J. P. Patau, T. Goulet, M-J. Fraser and J-P. Jay-Gerin, Monte Carlo simulation of fast electron and proton tracks in liquid water – I. Physical and physicochemical aspects. *Radiat. Phys. Chem.* **51**, 229–243 (1998)

10. Y. Frongillo, T. Goulet, M-J. Fraser, V. Cobut, J. P. Patau and J-P. Jay-Gerin, Monte Carlo simulation of fast electron and proton tracks in liquid water – II. Nonhomogeneous chemistry. *Radiat. Phys. Chem.* **51**, 245–254 (1998).

11. W. E. Wilson and H. Nikjoo, A Monte Carlo code for positive ion track simulation. *Radiat. Environ. Biophys.* **38**, 97–104(1999).

12. D. Emfietzoglou, G. Papamichael and M. Moscovitch, An event-by-event computer simulation of interactions of energetic charged particles and all their secondary electrons in water. *J. Phys. D Appl. Phys.* **33**, 932–944 (2000).

13. D. Emfietzoglou, G. Papamichael, K. Kostarelos and M. Moscovitch, A Monte Carlo track structure code for electrons (~10 eV–10 keV) and protons (0.3–10 MeV) in water: partitioning of energy and collision events. *Phys. Med. Biol.* **45**, 3171–3194 (2000).

14. S. Uehara, L. H. Toburen and H. Nikjoo, Development of a Monte Carlo track structure code for low-energy protons in water. *Int. J. Radiat. Biol.* **77**, 139–154 (2001).

15. H. Nikjoo, S. Uehara, D. Emfietzoglou and F. A. Cucinotta, Track-structure codes in radiation research. *Radiat. Meas.* **41**, 1052–1074 (2006).

16. M. Dingfelder, R. H. Ritchie, J. E. Turner, W. Friedland, H. G. Paretzke and R. N. Hamm, Comparisons of calculations with PARTRAC and NOREC: transport of electrons in liquid water. *Radiat. Res.* **169**, 584–594 (2008).

17. F. Ballarini, M. Biaggi, M. Merzagora, A. Ottolenghi, M. Dingfelder, W. Friedland, P. Jacob and H. G. Paretzke, Stochastic aspects and uncertainties in the prechemical and chemical stages of electron tracks in liquid water: a quantitative analysis based on Monte Carlo simulations. *Radiat. Environ. Biophys.* **39**, 179–188 (2000).

18. W. Friedland, P. Jacob, P. Bernhardt, H. G. Paretzke and M. Dingfelder, Simulation of DNA damage after proton irradiation. *Radiat. Res.* **159**, 401–410 (2003).

19. W. Friedland, M. Dingfelder, P. Jacob and H. G. Paretzke, Calculated DNA double-strand break and fragmentation yields after irradiation with He ions. *Radiat. Phys. Chem.* **72**, 279–286 (2005).

20. W. Friedland, P. Jacob, H. G. Paretzke, A. Ottolenghi, F. Ballarini and M. Liotta, Simulation of light ion induced DNA damage patterns. *Radiat. Prot. Dosimetry* **122**, 116–120 (2006).

21. W. B. Li, W. Friedland, E. Pomplun, P. Jacob, H. G. Paretzke, M. Lassmann and C. Reiners, Track structures and dose distributions from decays of ^{131}I and ^{125}I in and around water spheres simulating micrometastases of differentiated thyroid cancer. *Radiat. Res.* **156**, 419–429 (2001).

22. B. M. Sutherland, P. V. Bennett, O. Sidorkina and J. Laval, Clustered damages and total lesions induced in DNA by ionizing radiation: oxidized bases and strand breaks. *Biochemistry* **39**, 9026–8031 (2000).

23. B. M. Sutherland, P. V. Bennett, O. Sidorkina and J. Laval, Clustered DNA damages induced in isolated DNA and human cells by low doses of ionizing radiation. *Proc. Natl. Acad. Sci. USA* **97**, 103–108 (2000).

24. B. M. Sutherland, P. V. Bennett, H. Schenk, O. Sidorkina, J. Trunk, D. Monteleone and J Sutherland, Clustered DNA damages induced by high LET and low LET radiation, including heavy ions. *Phys. Med.* **XVII** (Suppl. I), 1–3 (2001).

25. A. G. Georgakilas, P. V. Bennett, and B. M. Sutherland, High efficiency detection of bi-stranded abasic clusters in γ-irradiated DNA by putrescine. *Nucleic Acids Res.* **30**, 2800–2808 (2002).

26. B. M. Sutherland, P. V. Bennett, J. Sutherland and J. Laval, Clustered DNA damages induced by X rays in human cells. *Radiat. Res.* **157**, 611–616 (2002).

27. M. Dingfelder, D. Hantke, M. Inokuti and H. G. Paretzke, Electron inelastic-scattering cross sections in liquid water. *Radiat. Phys. Chem.* **53**, 1–18 (1998).

28. M. Dingfelder, M. Inokuti and H. G. Paretzke, Inelastic-collision cross sections of liquid water for interactions of energetic protons. *Radiat. Phys. Chem.* **59**, 255–275 (2000).

29. F. Salvat, Optical model potential for electron and positron scattering by atoms. *Phys. Rev. A* **68**, 012708 (2003).

30. ICRU Report 77, *Elastic Scattering of Electrons and Protons. J. ICRU* **7** (2007).

31. W. Michaud, A. Wen and L. Sanche, Cross sections for low-energy (1–100 eV) electron elastic and inelastic scattering in amorphous ice. *Radiat. Res.* **159**, 3–22 (2003).

32. L. Sanche, Low energy electron-driven damages in biomolecules. *Eur. Phys. J. D* **35**, 367–390 (2005).

33. L. Sanche, Low-energy damage to DNA and its basic constituents. *Phys. Scripta* **T68**, C108–C112 (2003).

34. P. H. Cutler and J. C. Davis, Reflection and transmission of electrons through surface potential barriers. *Surf. Sci.* **1**, 194–212 (1964).

35. S. T. Manson, L. H. Toburen, D. H. Madison and N. Stolterfoht, Energy and angular distributions of electrons ejected by fast protons and electrons. *Phys. Rev. A* **12**, 60–79 (1975).

36. L. H. Toburen, Atomic and molecular physics in the gas phase. In *Physical and Chemical Mechanisms in Molecular Radiation Biology* (W. A. Glass and M. N. Varma, Eds.), pp. 51–97. Plenum Press, New York, 1991.

37. ICRU, *Stopping Powers and Ranges for Protons and Alpha Particles*. ICRU Report No. 49, International Commission on Radiation Units and Measurements, Bethesda, MD, 1993.

38. L. C. Northcliffe and R. F. Schilling, Range and stopping power tables for heavy ions. *Nucl. Data Tables* **7**, 233–463 (1970).

39. ICRU Report 73, *Stopping of Ions Heavier than Helium. J. ICRU* **5** (2005).

40. S. M. Pimblott, J. A. LaVerne and A. Mozumder, Monte Carlo simulation of range and energy deposition by electrons in gaseous and liquid water. *J. Phys. Chem.* **100**, 8595–8606 (1996).

41. C. G. Drexler and R. D. DuBois, Energy- and angle-differential yields of electron emission from thin carbon foils after fast proton impact. *Phys. Rev. A* **53**, 1630–1637 (1996).

42. C. G. Drexler, R. D. DuBois, H. G. Paretzke, and K-O. Groeneveld, Electron emission from condensed phase organic materials. In *Radiation Research 1895–1995*, Vol. 1, *Congress Abstracts* (U. Hagen, H. Jung and C. Streffer, Eds.), p. 110. Universitatsdruckerei H. Sturz AG, Würzburg, 1995.

43. R. D. DuBois and C. G. Drexler, Differential electron emission from solids and frozen gases. In *Proceeding of the 17th Werner Brandt Workshop on the Penetration of Charged Particles in Matter* (R. Baragiola, Ed.), pp. 95–104. University of Virginia, Charlottesville, 1997.

44. M. Dingfelder, A. Travia, R. A McLawhorn, J. L. Shinpaugh and L. H. Toburen, Electron emission from foils and biological materials after proton impact. *Radiat. Phys. Chem.* **77**, 1213–1217 (2008).

45. K. P. Stevenson, G. A. Kimmel, Z. Dohnálek, R. S. Smith and B. D. Kay, Controlling the morphology of amorphous solid water. *Science* **283**, 1505 (1999).

46. G. A. Kimmel, K. P. Stevenson, Z. Dohnálek, R. S. Smith and B. D. Kay, Control of amorphous solid water morphology using molecular beams. I. Experimental results. *J. Chem. Phys.* **114**, 5284–5294 (2001).

47. G. A. Kimmel, Z. Dohnálek, K. P. Stevenson, R. S. Smith and B. D. Kay, Control of amorphous solid water morphology using molecular beams. II. Ballistic deposition simulations. *J. Chem. Phys.* **114**, 5295–5303 (2001).

48. G. A. Kimmel, N. G. Petrik, Z. Dohnálek and B. D. Kay, Layer-by-layer growth of thin amorphous solid water films on Pt(111) and Pd(111). *J. Chem. Phys.* **125**, 1–12 (2006).

49. S. L. McLawhorn, R. A. McLawhorn, K. D. Carnes, P. Richard, M. Dingfelder, L. H. Toburen and J. L. Shinpaugh, Doubly differential electron yields from thin copper foils induced by fast ion impact. In *Application of Accelerators in Research and Industry: Proceedings of the Twentieth International Conference* (F. D. McDaniel and B. L. Doyle, Eds.), pp. 176–179. Conference Proceedings 1099, AIP Press, New York, 2009.

50. H. Lueth, *Surfaces and Interfaces of Solid Materials*, 3rd ed. Springer, Berlin, Heidelberg, New York, 1997.

51. J. L. Wiza, Microchannel plate detectors. *Nucl. Instrum. Methods* **162**, 587–601 (1979).

52. L. H. Toburen, Distributions in energy and angle of electrons ejected from molecular nitrogen by 0.3- to 1.7-MeV protons. *Phys. Rev. A* **3**, 216–228 (1971).

53. A. Müller, N. Djurić, G. H. Dunn and D. S. Belić, Absolute detection efficiencies of microchannel plates for 0.1–2.3 keV electrons and 2.1–4.4 keV Mg$^+$ ions. *Rev. Sci. Instrum.* **57**, 349–353 (1986).

54. A. Koyama, T. Shikata and H. Sakairi, Secondary electron emission from Al, Cu, Ag, and Au, by proton impact. *Jpn. J. Appl. Phys.* **20**, 65–70 (1981).

55. L. H. Toburen and W. E. Wilson, Time-of-flight measurements of low energy electron energy distributions from ion-atom collisions. *Rev. Sci. Instrum.* **46**, 851–854 (1975).

56. C. D. Wilson, C. A. Duke and R. A. Baragiola, Search for the plasmon in condensed water. *Phys. Rev. B* **63**, 121101 1–4 (2001).

57. G. Schiwietz, K. Czerski, M. Roth, F. Staufenbiel and P. L. Grande, Femtosecond dynamics – snapshots of the early ion-track evolution. *Nucl. Instrum. Methods B* **226**, 683–704 (2004)

58. N. V. Neelavathi, R. H. Richie and W. Brandt, Bound electron states in the wake of swift ions in solids. *Phys. Rev. Lett.* **33**, 302–305 (1974).

59. L. H. Toburen, R. D. DuBois, C. O. Reinhold, D. R. Schultz and R. E. Olson, Experimental and theoretical study of the electron spectra in 66.7–350-keV/u C$^+$ + He collisions. *Phys. Rev. A* **42**, 5338–5347 (1990).